Science Advances
AAAS

Supplementary Materials for

Atomically sharp domain walls in an antiferromagnet

Filip Krizek*, Sonka Reimers, Zdeněk Kašpar, Alberto Marmodoro, Jan Michalička, Ondřej Man, Alexander Edström, Oliver J. Amin, Kevin W. Edmonds, Richard P. Campion, Francesco Maccherozzi, Samjeet S. Dhesi, Jan Zubáč, Dominik Kriegner, Dina Carbone, Jakub Železný, Karel Výborný, Kamil Olejník, Vít Novák, Jan Rusz, Juan-Carlos Idrobo, Peter Wadley, Tomas Jungwirth*

*Corresponding author. Email: krizekfi@fzu.cz (F.K.); jungw@fzu.cz (T.J.)

Published 30 March 2022, *Sci. Adv.* **8**, eabn3535 (2022)
DOI: 10.1126/sciadv.abn3535

This PDF file includes:

1 Magnetic-field generating objective lenses in STEM

The simultaneous measurement of HAADF and DPC at high resolution requires active objective lenses, which generate a magnetic field of about 1.5 T aligned perpendicular to the lamella. This would limit DPC-STEM domain wall measurements of most ferromagnetic materials. Antiferromagnets, in general, are significantly less sensitive to magnetic fields. Moreover, a magnetic field does not displace a 180° domain wall in an antiferromagnet, since the two opposite Néel vector domains have the same Zeeman energy. For our atomically sharp 180° domain walls containing no internal structure with intermediate magnetic moment angles, the effect of an external magnetic field on the domain wall is further diminished. The field could only change the angle of the Néel vectors in the two domains while keeping their mutually opposite orientation. Here the preferred angle is along an axis orthogonal to the applied field, for field strengths above the rotation (spin-flop) threshold. In earlier reports, this threshold has been estimated to approximately 2 T in CuMnAs (*8*). In our geometry, this would correspond to the rotation of the opposite Néel vectors in the two domains within the CuMnAs (001) easy plane closer to the direction orthogonal to the electron beam. The magnetic field can, therefore, have either no or a favorable effect in our DPC-STEM measurements.

2 XMLD-PEEM detection limit in CuMnAs

The detection limit for magnetic textures using XMLD-PEEM depends on the instrument resolution, signal-to-noise ratio and pixel size. We estimate a signal-to-noise ratio of ≈ 15 from line-scans taken across the ≈ 100 nm wide 180° domain walls seen in bottom part of Fig. 2a of the main text. To estimate the detection limit, we simulate images of a domain wall using a Gaussian profile with full-width half-maximum f, convoluted with the known instrumental broadening of 30 nm and the measured signal-to-noise ratio, and sampled with the same pixel size. Results are shown in Supplementary Fig. S1 for domain walls with f ranging from 200 to 5 nm. While a 10 nm wide domain wall is still detectable, we lose the contrast for a 5 nm domain wall.

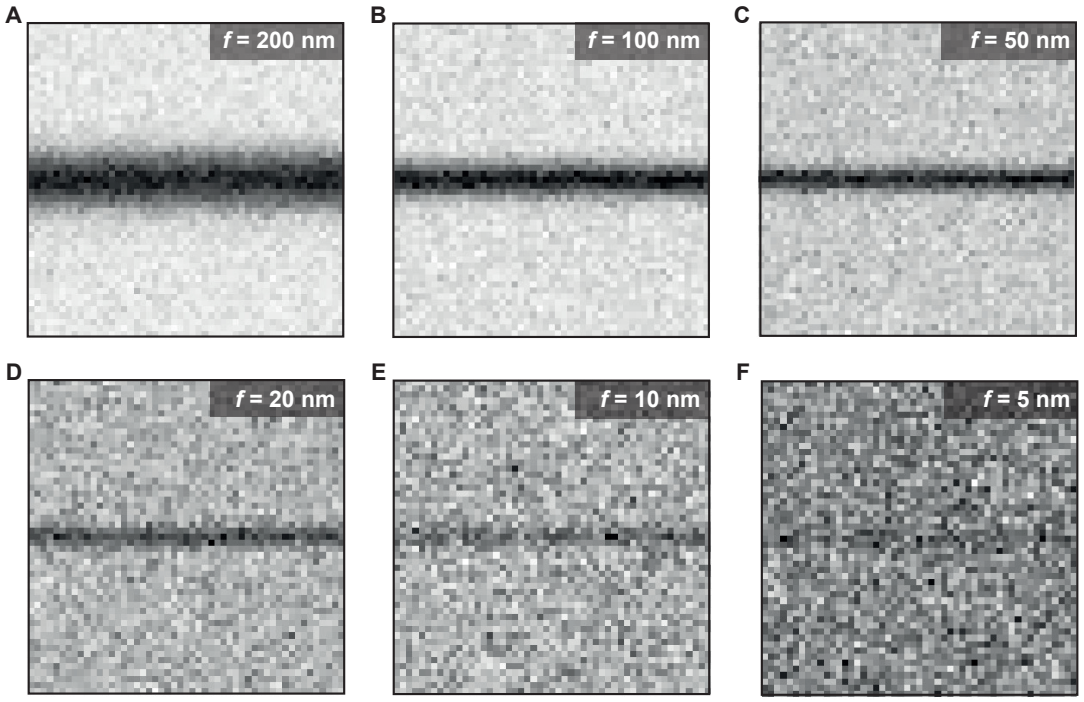

Figure S 1: Simulated images of 180° domain walls with varying full-width half-maximum *(f)*. (**A**) $f = 200$ nm. (**B**) $f = 100$ nm. (**C**) $f = 50$ nm. (**D**) $f = 20$ nm. (**E**) $f = 10$ nm. (**F**) $f = 5$ nm. The image sizes are 1.3×1.3 μm.

3 XMLD-PEEM imaging in CuMnAs

A common perception of the dipole-free antiferromagnets had been that the stable states should be single-domain without the presence of higher-energy magnetic textures. However, magnetic imaging measurements in the antiferromagnetic CuMnAs epilayers evidenced the presence of stationary magnetic textures on a broad range of length-scales (*7, 20, 22, 23, 41*). These earlier experiments are summarized in Sec. "XMLD-PEEM imaging" in the main text.

In Supplementary Fig. S2 we show additional XMLD-PEEM and X-ray absorption measurements illustrating pinning of an unresolved origin, and reversible electrical manipulation of ≈ 100 nm wide 180° domain walls, extending in length over several microns with no preferred orientation with respect to the crystal. The experiment illustrates that while stationary in the absence of external stimuli, the domain walls are not necessarily permanently fixed by an (unknown) structural pinning defect and can be manipulated in a controlled way, e.g., by switching the polarity of the driving current pulses.

From the XMLD-PEEM measurements shown in Fig. 2 in the main text we then infer the presence of 180° Néel vector reversals on an unexpectedly small scale below the ≈ 10 nm detection limit of XMLD-PEEM. The inability to determine the microscopic morphology of these

small-scale antiferromagnetic textures by the established XMLD-PEEM technique directly motivated our DPC-STEM study.

The collection of imaging results by XMLD-PEEM in CuMnAs counters the common perception that antiferromagnets should display single domain states because there is no long-range magnetic dipole field dictating the stable domain structure. On contrary, the XMLD-PEEM results evidence that the antiferromagnetic CuMnAs epilayers have a strong tendency to form complex stationary multi-domain (multi domain-wall) textures on a broad range of length-scales from above microns to below the ≈ 10 nm detection limit of XMLD-PEEM. Our understanding is that, once the more complex magnetic texture is generated at non-equilibrium conditions during synthesis or after growth by external stimuli, the lack of the long-range dipole fields inhibits efficient removal of the textures and makes them more stationary. Also, unlike the coarse-graining global molecular field in ferromagnets, the local nature of the molecular field in antiferromagnets makes their magnetic textures more sensitive to local perturbations in the crystal. As a result, the microscopic defects in the high-quality single-crystal epilayers of CuMnAs, which can pin the domain walls and stabilize the complex antiferromagnetic textures, are not sufficiently pronounced to be detectable by the available microscopy technique.

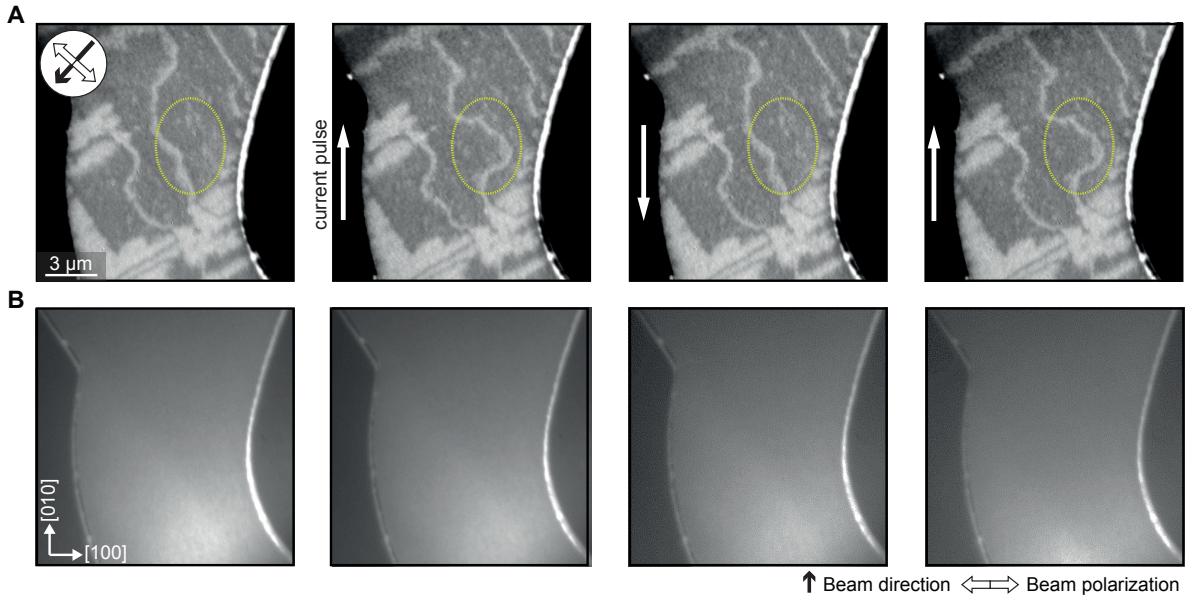

Figure S 2: XMLD-PEEM imaging of ≈100 nm wide 180° domain walls in a CuMnAs epilayer. (**A**) XMLD-PEEM images of a reversible and reproducible displacement of a 180° domain wall (circled by a yellow dashed line), controlled by the polarity of an applied electrical current of $\approx 5 \times 10^6$ Acm^{-2}. (**B**) X-ray absorption PEEM shows no detectable crystal pinning defect. The white arrows in XMLD-PEEM images indicate the polarity of the current-pulses.

4 DFT-based Pauli multi-slice DPC-STEM simulations

Atomic scale DPC images are directly interpretable only at extremely low sample thicknesses and for sufficiently large collection angles (*24*). In these conditions, the magnetic component of the DPC signal starts as an expected weak fraction of the total DPC signal. This is due to weaker interaction of electrons with magnetic fields when compared to the Coulomb potentials (*19*). By reducing the collection angle and increasing sample thickness, the DPC images quickly lose their quantitative and even qualitative interpretability due to pronounced dynamical diffraction effects (*24, 42*). Yet, perhaps paradoxically at the first sight, this complexity of dynamical diffraction effects can be of advantage for magnetic imaging. Fractionally small initial differences of DPC signals due to opposite magnetic moments in two antiferromagnetic domains will get gradually enhanced by dynamical diffraction effects, as the sample thickness increases, leading to an enhanced magnetic signal fraction. The loss of interpretability of the spatial distribution of DPC signal can be thus traded for a higher sensitivity to the presence and qualitative changes of magnetism. To verify these points in CuMnAs, which guided our approach to the DPC-STEM measurements, we performed state-of-the-art Pauli multislice STEM-DPC simulations.

The simulations were performed on a grid of 32 x 16 beam positions, considering a convergent probe with convergence semi-angle of 25 mrad and acceleration voltage of 100 kV. A static lattice model has been used here. Unit cell was sampled on a grid of 128 x 64 pixels and 32 slices were generated per unit cell along the beam direction. The supercell for STEM simulations consisted of 16 x 24 unit cells in lateral directions.

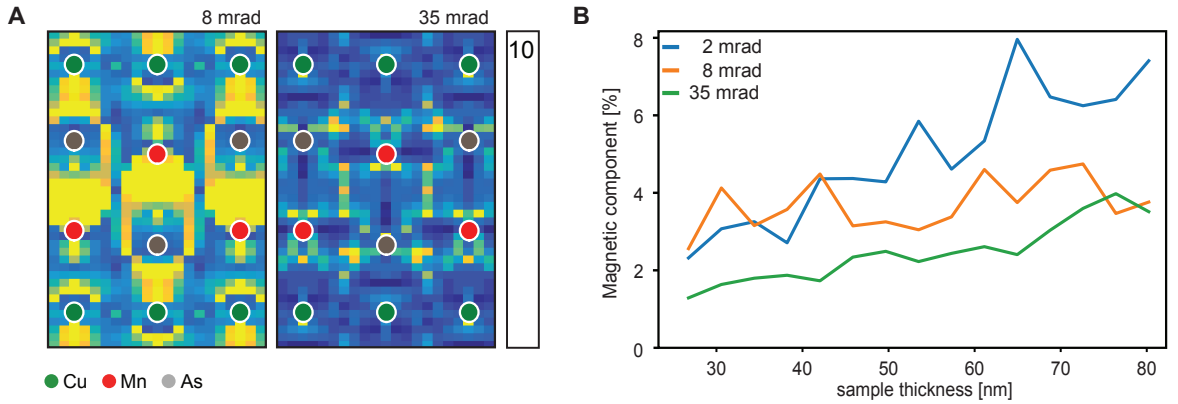

Figure S 3: **Pauli multi-slice DPC-STEM simulations.** (**A**) Simulation of the distribution of the relative strength of the magnetic component with respect to the total DPC-STEM signal. The color scale is limited to 10%. The atomic positions are highlighted by green/Cu, red/Mn, grey/As. (**B**) Simulated dependence of the relative strength of the magnetic component of the DPC-STEM signal on sample thickness for three different sizes of the ronchigram mask.

The internal magnetic and electric fields used in the Pauli multi-slice DPC-STEM simulations were obtained from the DFT calculations (*19, 43–45*). Within an 0.3 Å thin slice of the CuMnAs unit cell centered around a selected plane of Mn atoms, an average internal magnetic field approaches ± 6 T (with ± 3.65 μ_{B} per Mn). A maximum projected internal field within a column of an 0.3 Å diameter around a selected Mn atom reaches 20 T. Further insight into the magnitudes of microscopically varying internal fields in other systems can be found, e.g., in Refs. (*44, 45*).

The magnetic component of the DPC signal was extracted as a difference of center of mass vectors extracted from two simulations with mutually reversed magnetizations. For a small mask (8 mrad), the simulations in Supplementary Fig. S3A show a significant relative contribution from the magnetic component in large portions of the CuMnAs unit cell, while a large mask (35 mrad) makes the local magnetic component less visible within the unit cell. Simulations shown in Supplementary Fig. S3B also confirm that a smaller mask combined with lamella thicknesses above 50 nm, as used in our experiments, are favorable for making the magnetic component of the DPC-STEM signal locally more prominent within the unit cell. The scale of the simulated total DPC signal is $\sim 0.1 - 1$ mrad.

5 DPC-STEM images from a pixelated detector and smaller or larger digital masks, and from a 4-quadrant detector

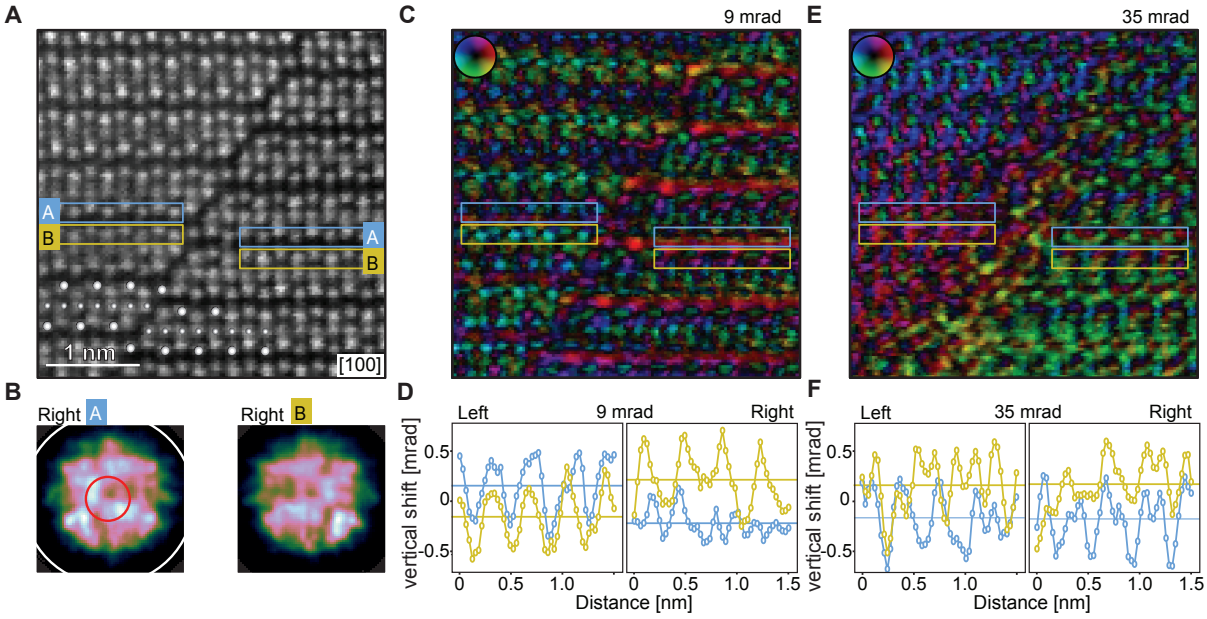

Figure S 4: Additional data on the DPC-STEM measurement from Fig. 3 of the main text. (**A**) Same as Fig. 3A in the main text. (**B**) Recorded ronchigrams integrated over the areas highlighted in A. Red circle highlights a 9 mrad-radius digital aperture mask, while the white circle corresponds to a 35 mrad mask. (**C**) Same as Fig. 3B in the main text. (**D**) Same as the bottom-left and top-right line-scans in Fig. 3C,D in the main text. (**E**) Same as C for a 35 mrad mask. (**F**) Same as D for a 35 mrad mask.

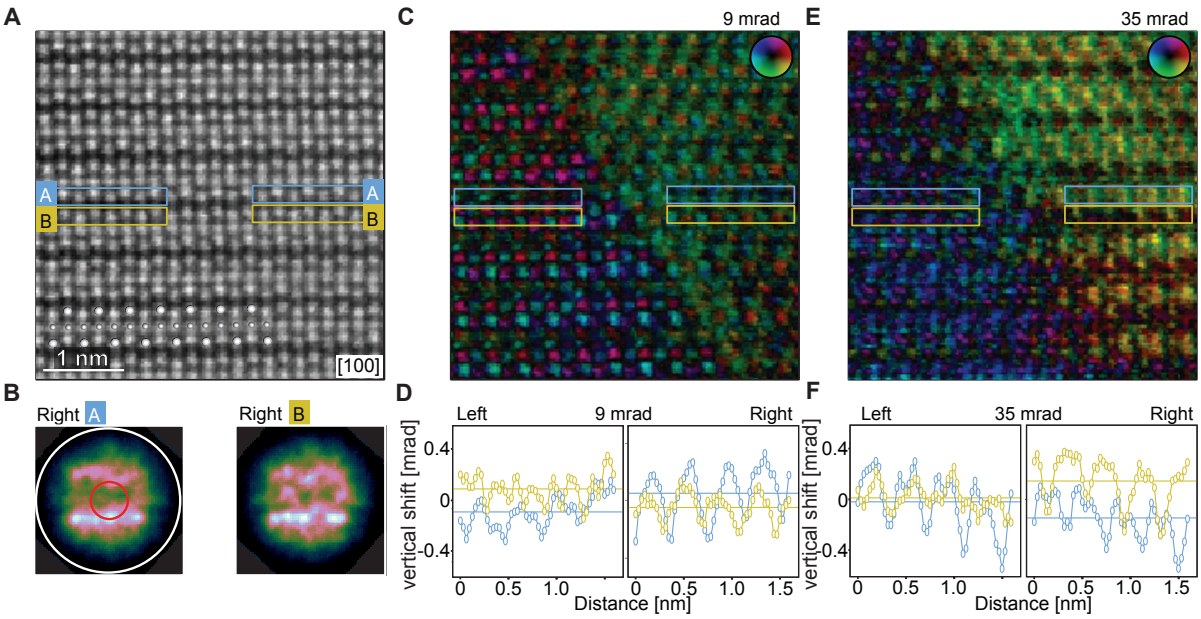

Figure S 5: Additional data on the DPC-STEM measurement from Fig. 4 of the main text.(**A-F**) Same as A-F in Supplementary Fig. S4, corresponding to Fig. 4 of the main text

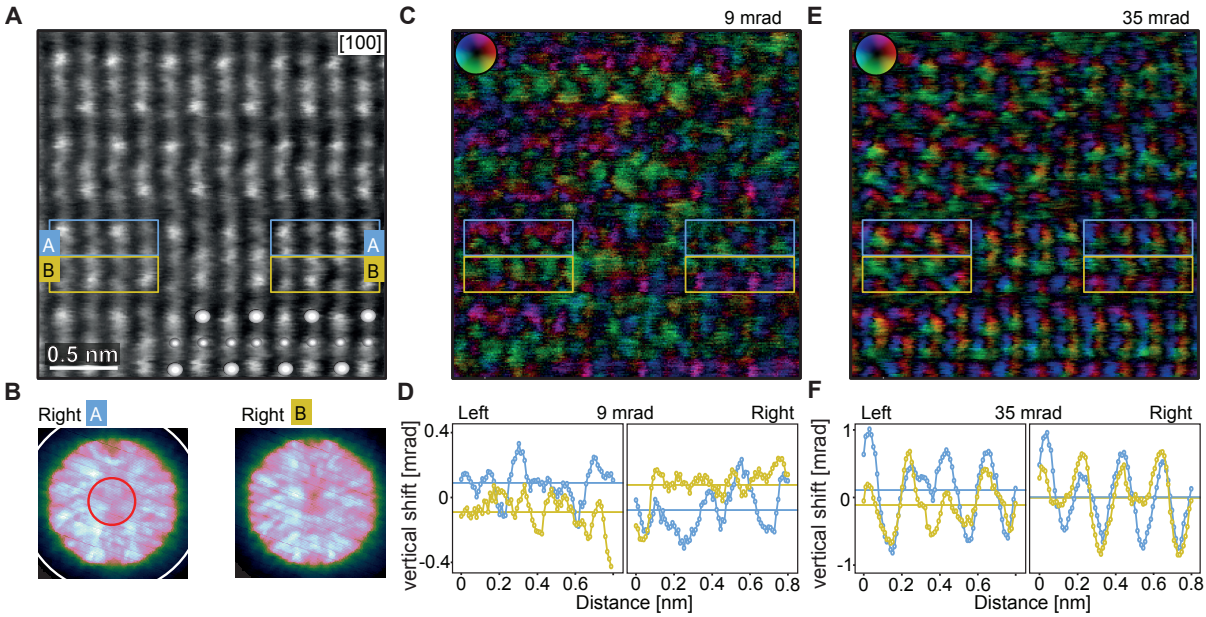

Figure S 6: Additional DPC-STEM measurement of an atomically sharp domain wall in a CuMnAs single-crystal. (**A-F**) Analogous data to Supplementary Fig. 5A-F for another domain wall in a part of the CuMnAs epilayer without a detectable crystal defect, obtained by employing Jeol STEM instrument (see Materials and Methods).

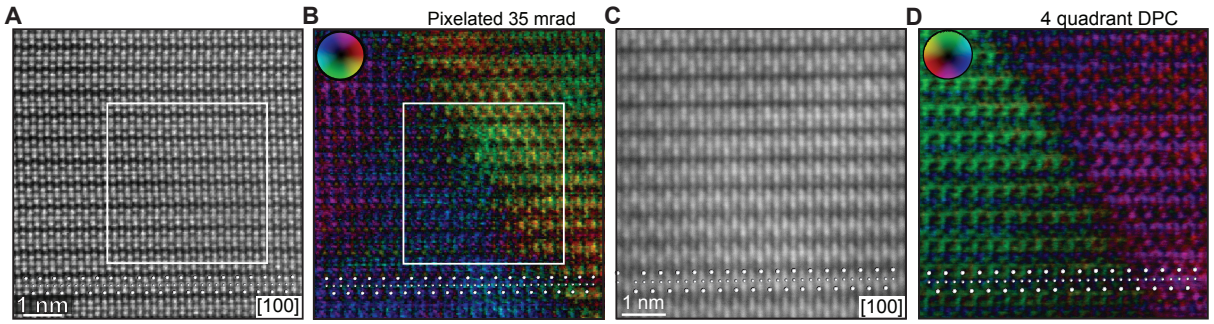

Figure S 7: **Larger field of view images of atomically sharp domain walls in a CuMnAs single-crystal.** (**A,B**) Zoom-out version of the same measurement as shown in Supplementary Fig. 5A,E. The area corresponding to images shown in Supplementary Fig. 5A,E is highlighted by a white rectangle. (**C**) Titan Themis (see Materials and Methods) HAADF-STEM micrograph of a CuMnAs single-crystal. (**D**) Corresponding 4-quadrant DPC-STEM image showing a sharp contrast on opposite sides of an abrupt domain wall.

6 DPC-STEM images of strained CuMnAs/GaP and CuMnAs/GaAs interfaces

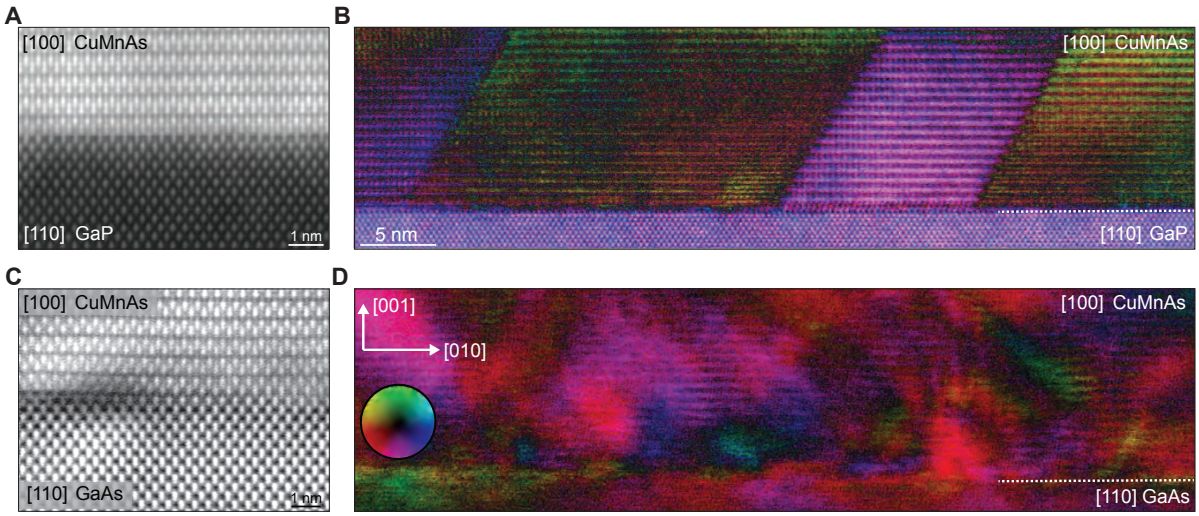

Figure S 8: Strain effects in CuMnAs/GaP and CuMnAs/GaAs. (**A**) HAADF-STEM im-age of a [100] projection of the epitaxial 50 nm thick CuMnAs film grown on lattice-matched GaP. (**B**) DPC-STEM image of the atomically sharp domain walls in the CuMnAs/GaP film.(**C**) HAADF-STEM image of the interface between 50 nm thick CuMnAs layer and a GaAs substrate (*26*). Distortions attributed to the presence of misfit dislocations and strain fields are apparent in both the epilayer and the substrate. (**D**) DPC-STEM image of the CuMnAs/GaAs layer, showing gradual changes in contrast on both sides of the epilayer/substrate interface due to the presence of strain fields.

7 Stoichiometry, thickness, and crystal rotation measurements and simulations

7.1 Electron energy loss spectroscopy measurements

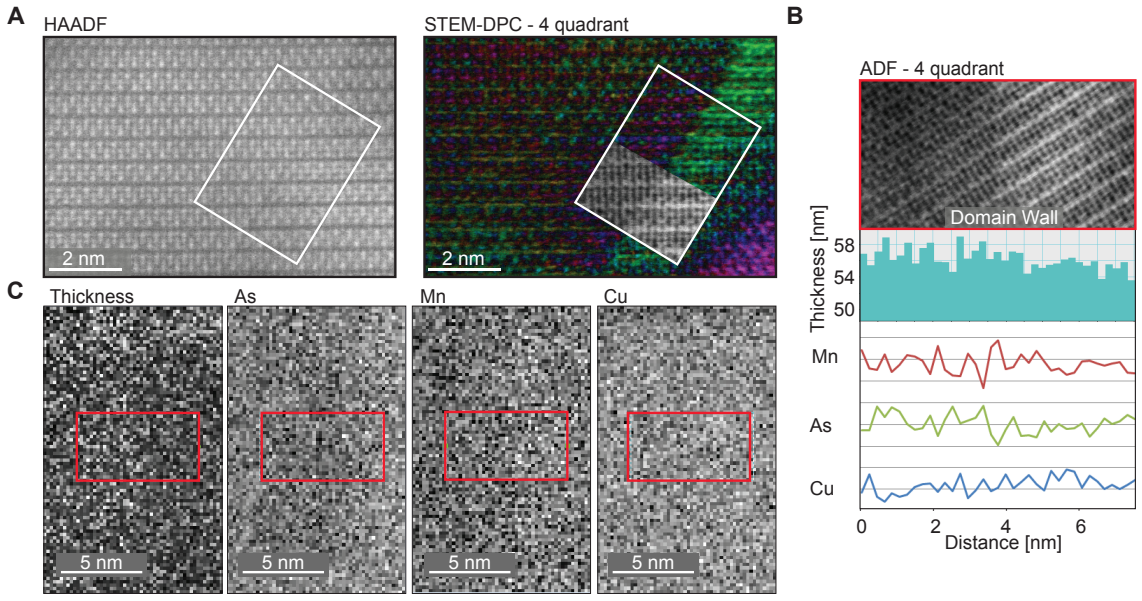

Figure S 9: Stoichiometry and thickness measurements. (**A**) HAADF-STEM image of a pristine CuMnAs crystal is shown in the left panel. Corresponding DPC-STEM measurement showing a sharp domain wall is presented in the right panel. The area highlighted by the white rectangle contains an inset with an image formed by summing the signals from all segments of the 4-quadrant DPC detector, i.e., the DPC detector is used as an annular bright field (ABF) detector which highlights the atomic position of the domain wall. Electron energy-loss spectroscopy (EELS) measurements were also performed in this area (as shown in (B)). (**B**) Horizontal line profile of absolute thickness of the sample across the region (highlighted by red rectangle) and perpendicular to the domain wall. The thickness is calculated from a low-loss EELS spectrum image via the Log-ratio method (*46*) and it shows no abrupt change over the domain wall. The red, green and blue intensity profiles of Mn-$M_{2,3}$, As-$M_{4,5}$ and Cu-$M_{2,3}$ edges extracted from the acquired EELS spectral image and used for profile measurements in the lower panel. The acquired element distributions confirm homogeneous distribution of Mn, As, and Cu across the domain wall. (**C**) The full spatial intensity distribution of values obtained from the EELS spectrum image and used for profiles in (B).

7.2 Multislice simulations of structural effects

To simulate the effects of thickness, defocus, and tilt on HAADF and DPC-STEM images of CuMnAs at atomic resolution, we have employed the DrProbe package (*25*), which implements conventional multi-slice simulations combined with the frozen phonon method. A supercell of lateral dimensions of approximately 5×5 nm^2 has been constructed (consisting of 8×13 unit cells with dimensions $a = 0.6318$ nm and $c = 0.3820$ nm). In total, 50 different frozen phonon configurations have been generated using an Einstein model and an approximate Debye-Waller factor of 0.01 nm^2. Convergence semi-angle of 25 mrad and acceleration voltage of 100 kV have been assumed, following the experimental parameters using the Nion UltraSTEM. Aberration coefficients were all set to zero, assuming a high-quality aberration correction. Only the defocus parameter has been varied in the first part of the simulations to estimate the most likely position of the focal plane in experiments. HAADF and DPC images were calculated over a single unit cell sampled by 32×19 beam positions, corresponding to an approximate distance of 0.02 nm between scan points. Sample thicknesses of up to $\approx$ 40 nm have been considered. In the HAADF calculations we have assumed an inner and outer collection semi-angles of 100 and 250 mrad, respectively. In the DPC simulations, the center of mass of the diffraction pattern has been calculated for a scattering angle cut-off of 8 mrad, as in the experiments shown in the main text for the smaller ronchigram mask.

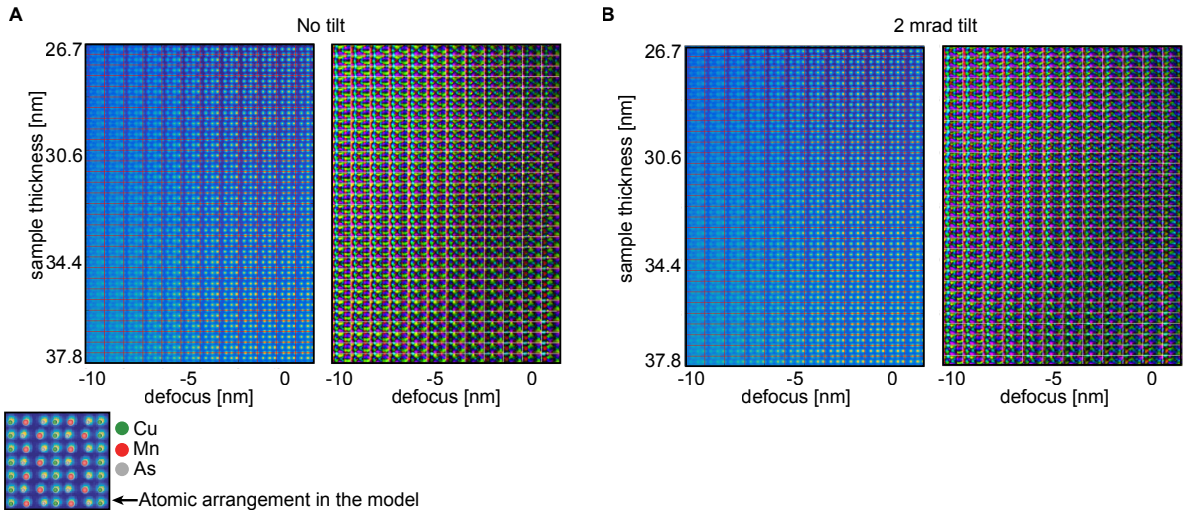

Figure S 10: Frozen phonon multislice calculations: thickness, defocus and tilt. (**A**) Frozen phonon multislice calculations of HAADF (left) and DPC-STEM (right) images of CuMnAs at 100 kV and 25 mrad convergence semi-angle and an electron beam exactly parallel to the zone axis. Red grid lines in the HAADF and white grid lines in the DPC image delineate regions of individual unit cells, each calculated for a different combination of sample thickness and defocus, as is indicated by axis labels. (**B**) The same as in A but with incoming beam tilted by 2 mrad from the zone axis.

In the first step, we have calculated thickness-defocus tableaux, shown in Supplementary Fig. S10A. From the simulations one can conclude: i) The defocus parameter, conventionally set in experiment to maximize the contrast in HAADF, must have been set to a value close to zero, i.e., with focal plane close to the entrance plane of the sample surface. ii) The individual images vary relatively slowly as a function of both thickness and defocus parameter. Therefore, any hypothetical thickness step (up to 3 nm in size) at the domain boundary cannot explain the large qualitative difference observed in the measured DPC images between the two domains.

Another considered structural effect is the sample tilt. We have addressed a question, whether an eventual relative crystal tilt of the two sides separated by the sharp domain wall could potentially explain the large differences seen in the measured DPC images. For that purpose, we have repeated the simulations discussed in the previous paragraph, however this time with an incoming electron beam tilted by approximately 2 mrad from the zone axis. The results are summarized in Supplementary Fig. S10B. The HAADF images are practically indistinguishable from the calculations with beam parallel to the zone axis. This matches well with the expected robustness of HAADF images with respect to small tilts. A qualitative explanation is based on the electron channeling phenomenon which overcomes the small tilt when the focused electron beam enters the sample in a close neighborhood of an atomic column. The simulated DPC image with a tilt also shows only a minor difference from the simulation where the beam was set parallel to the zone axis. The differences in simulations are substantially smaller than the qualitative changes of the experimental domain wall DPC images. Therefore we conclude that a hypothetical small relative crystal tilt also cannot explain the larger differences in DPC images observed in experiment.

7.3 Crystal overlap measurements and simulations

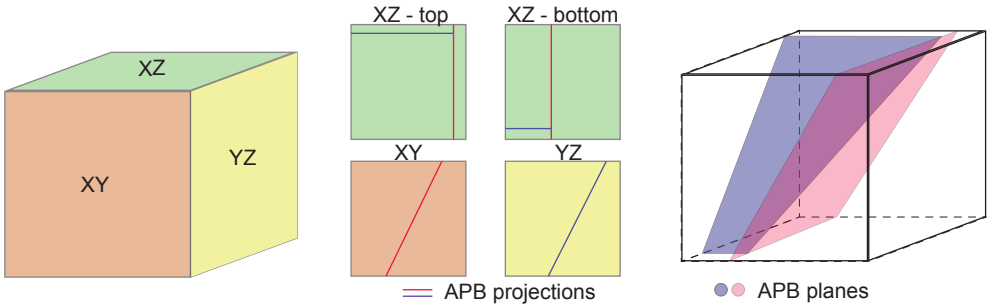

Figure S 11: Crystal overlap schematics. Illustration of the formation of possible crystal overlaps in tetragonal CuMnAs thin films. Here two anti-phase boundary defects meet within the layer and form a gradual overlap, i.e., would project as vertical gradients in the HAADF-STEM images, observable from both XY [100] and YZ [010] projections of the crystal.

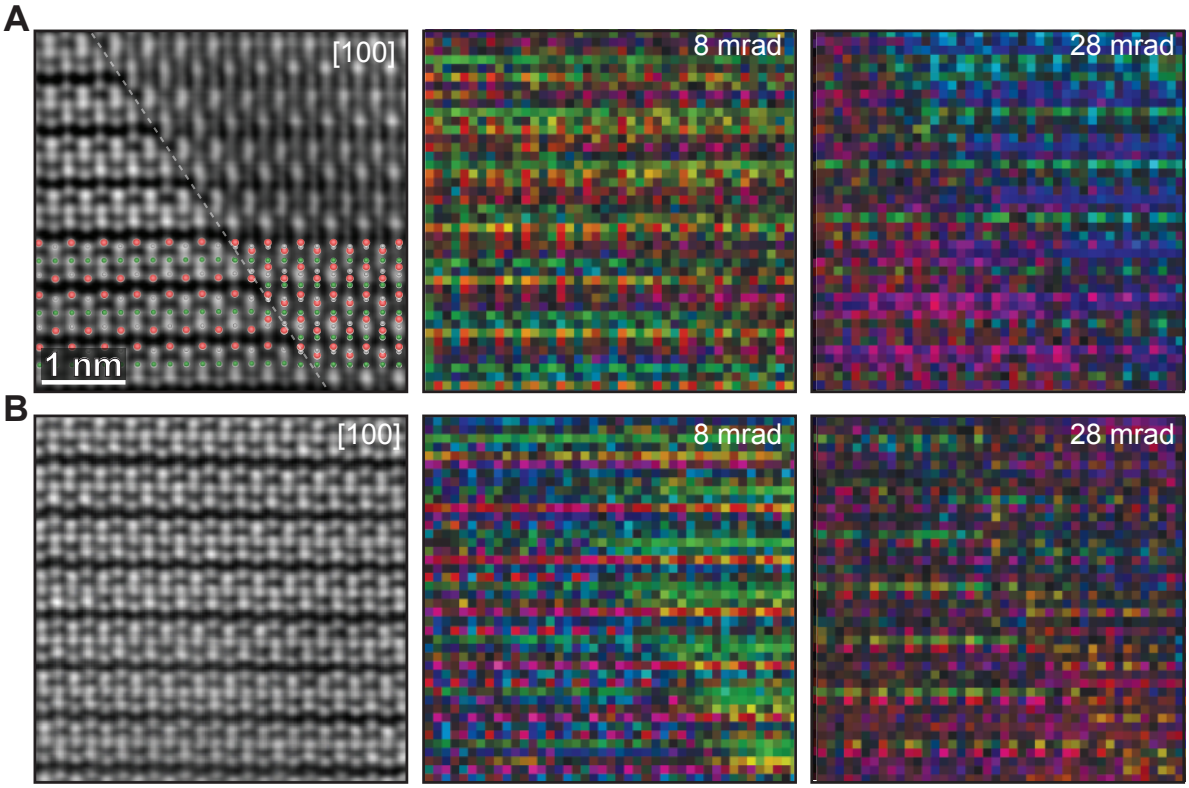

Figure S 12: STEM measurement of the crystal overlap. (**A**) HAADF-STEM image (left panel) showing an interface between a pristine CuMnAs crystal and a projection of an overlap region. The overlap is due to anti-phase boundaries formed along different $\{011\}$ planes, as illustrated in Supplementary Fig. S11. The two corresponding DPC-STEM images highlight that the DPC contrast due to the overlap is partially suppressed when processing the data with a smaller radius ronchigram mask. (**B**) Same as (A) but measured in a structurally unperturbed part of the crystal containing the atomically sharp domain wall. The DPC-STEM image shows an opposite trend to (A) with a stronger contrast appearing for the smaller mask. This is consistent with the presence of the antiferromagnetic domain wall, shown in Fig. 1D of the main text.

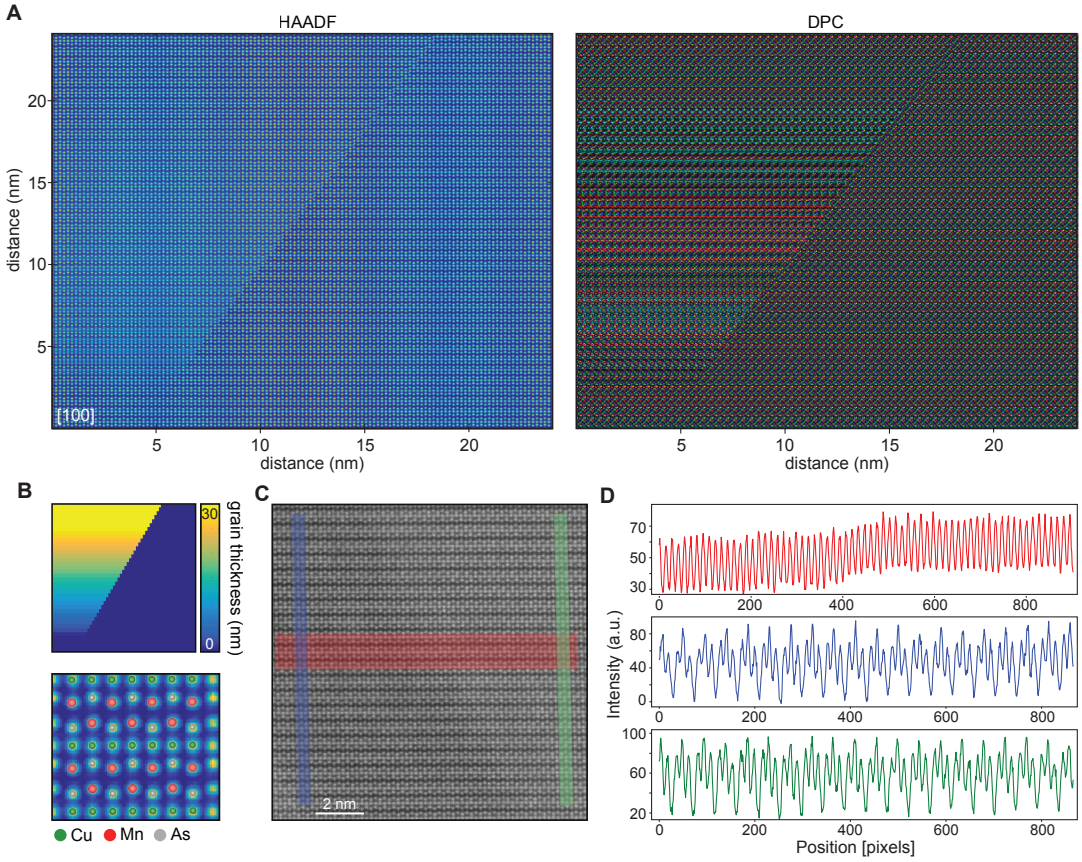

Figure S 13: Crystal overlap simulation compared with measurements of an unperturbed portion of the crystal featuring the sharp domain wall. (**A**) Frozen-phonon multi-slice simulations (see Supplementary Sec. 7.2) of HAADF and DPC-STEM images of a crystal overlap defect, showing contrast modulation in the vertical direction due to the gradually varying relative thickness between the two overlapping crystals. (**B**) The morphology of the crystal overlap defect considered in the simulations, respecting the crystallographic properties of the anti-phase boundaries (see Supplementary Fig. S11). (**C**) Larger field of view of the experimental HAADF-STEM image shown in Fig. 4A of the main text, corresponding to the region with the sharp domain wall seen in the DPC-STEM image in Fig. 4B of the main text. (**D**) Vertical and horizontal intensity line profiles extracted from (C). The vertical profile directions run from top to bottom. The vertical intensity line profiles do not show any gradient. The horizontal profile in (C) shows a small step in the intensity. Similarly to the DPC contrast, we found no indication that this slight change in contrast is related to common structural origins of contrast in HAADF-STEM images like, for example, the redistribution and/or change of atomic species, stoichiometry, thickness, rotation, or crystal overlap. Therefore, we surmise, that it is related to an asymmetry which, instead of a crystallography origin, is caused by the presence of the opposite antiferromagnetic domains separated by the sharp magnetic domain wall.

8 Calculations of the energy of narrow domain walls in CuMnAs

8.1 Atomistic Heisenberg model simulations

We use the atomistic spin dynamics code SPIRIT (*47*) to simulate narrow domain walls of varying width within the semiclassical Heisenberg model. For these simulations we consider a system composed of $20 \times 1 \times 1$ unit cells with periodic boundary conditions along the [010] and [001] directions. The domain wall width is parametrized by the reorientation angle θ between adjacent magnetic layers inside the domain wall (see Supplementary Fig. S14A). We use exchange parameters of bulk CuMnAs calculated via the magnetic-force theorem (*48*) using the Korringa, Kohn, Rostoker scheme in the implementation of the spin polarized relativistic KKR (SPRKKR) package (*49*). We include a uniaxial anisotropy along the [001] direction of 0.1 meV per Mn, forcing the moments to stay in the (001)-plane, and a cubic anisotropy of 0.01 meV per Mn to simulate the in-plane anisotropy. Since we study the domain walls in the narrow regime where the energy is exchange dominated, the magnitudes of the anisotropy terms do not significantly influence the result.

The red curve in Supplementary Fig. S14B shows the dependence of the domain wall energy on the domain wall width parametrized via θ. This dependence is similar to the result for the simplest case of a 1D ferromagnetic or antiferromagnetic chain with nearest neighbor exchange interactions. We find that the energy is increasing with decreasing width and, like in the 1D chain case, we also find that the two narrowest domains have the same energy. In the Heisenberg model with a cosine dependence of the exchange energy on the angle between neighboring spins, the atomically sharp domain wall with one neighboring spin aligned with the exchange field and another one aligned against the field has the same energy as the second narrowest domain wall with the neighboring moments pointing in the orthogonal direction.

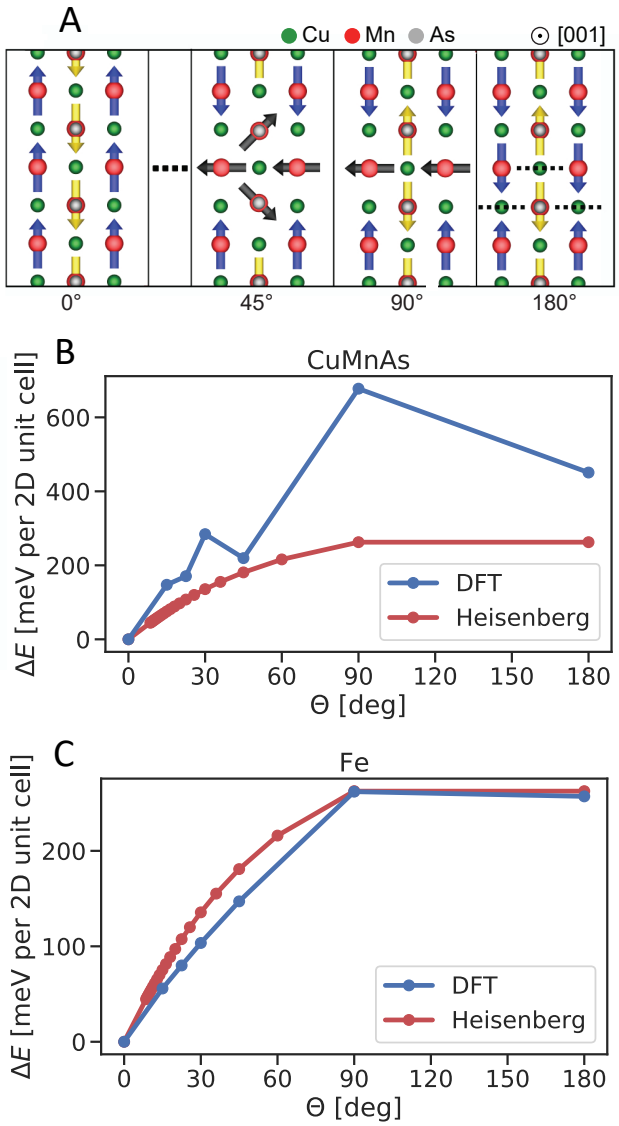

Figure S 14: Calculations of the energy vs. width of narrow domain walls. (**A**) Schemat-ics of the Mn magnetic moment alignment (arrows) in CuMnAs for the first, second, and third narrowest domain wall and for the uniform single-domain antiferromagnetic state. An analogous model was considered for Fe, but only with the corresponding ferromagnetic order in the domains. (**B**) Self-consistent-field density-functional-theory calculations (blue) and atomistic semiclassical Heisenberg model simulations (red) of the energy of the domain wall in CuMnAs, with respect to the energy of a uniform single-domain state, as a function of its width, parametrized by the reorientation angle between adjacent magnetic layers inside the domain wall. The energy is plotted per 2D unit cell in the plane of the domain wall. (**C**) Same as B for Fe.

We note that in the 1D chain model, the configuration of spins within a domain wall of a given width is such that all angles between adjacent magnetic layers across the domain wall are equal. In our Heisenberg simulations of CuMnAs we find that this is also quite closely satisfied. We note that for the second narrowest domain wall with a single layer of tilted spins, the choice of the tilt angle within the Heisenberg model is arbitrary since all angles give the same energy. The red curve in Supplementary Fig. S14C shows an analogous result in ferromagnetic Fe.

8.2 Self-consistent-field density-functional-theory calculations

The self-consistent-field density-functional-theory (SCF-DFT) calculations were performed in terms of the four-component Dirac electronic Hamiltonian (*50, 51*), which includes relativistic effects non-perturbatively. For its Green function solution, we have resorted to the SPRKKR package (*49*). Adoption of the local spin density approximation (LSDA) exchange-correlation functional by Vosko, Wilk and Nusair (*52*) and of the atomic sphere approximation have been previously found adequate to reproduce CuMnAs experimental trends for ground state magnetism, Néel transition temperature, and charge transport (*27, 53*), already at the linearized muffin-tin orbitals (LMTO) level (*54*). These approximations have also shown a good agreement with ab initio results produced by very different computational frameworks such as the plane wave basis set and the pseudopotential scheme implemented within the Vienna ab-initio simulation package (VASP) (*55*), as well as the fully relativistic linear combination of atomic orbitals (LCAO) scheme by the full-potential local orbital (FPLO) package (*56*). We use experimental lattice parameters from thin film X-ray diffraction measurements (*57*) and include an additional $2c$ Wyckoff position for two supplementary empty sphere sublattices, to improve convergence of the multiple scattering expansion.

For our domain wall study we examine the situation of two semi-infinite regions with opposite antiferromagnetic long range orders (LROs), which meet in the middle through a Néel-like domain wall. We assume the $[100]$ direction as the reference orientation for the Néel vector, and consider a domain wall in the (100)-plane, within which both atomic moments of the two Mn sublattices rotate until the full recovery of LRO and with the Néel vector in the left region pointing along the $[100]$ direction and in the right region along the $[\bar{1}00]$ direction. The domain wall width is then defined by the number of manganese atoms over which the above rotation takes place, and parametrized by the rotation angle θ in the above semiclassical Heisenberg model simulations. In order to efficiently describe the domain wall as an extended defect, we have resorted to a 2D tight-binding KKR calculation scheme (*58, 59*), which enables a detailed computational study of a finite 2D periodic inner portion of the system (interaction zone) embedded within two semi-infinite 3D periodic (left and right) regions. This numerical framework is deployed onto a fixed interaction zone thickness of 38.2 Å along the [100] direction, corresponding to 10 CuMnAs unit cells and verified to be adequately large for smooth matching of the embedding self-energy to the left and right semi-infinite regions, with their SCF-DFT ground states previously computed as 3D periodic and subsequently pinned.

In the absence of any deviation from magnetic LRO, i.e., the same orientation throughout

the interaction zone as well as within the left and right semi-infinite regions, the setup reproduces well-established bulk results for all site-diagonal quantities, such as the density of states and the layer-projected spin-polarized charge density; and provides in particular a reference value for the total energy. Upon setting up the left and right regions with opposite Néel vector orientations, and re-converging the system with the spin magnetic moments of the interaction zone set up to complete the 180° rotation along the [100] direction, we obtain a new total energy for each trial scenario. The difference with respect to the LRO case provides a definition for the energy cost of the domain wall as a function of its width, from the most abrupt scenario to a thickness spanning 11 Mn atoms along the [100] direction.

Due to the choice of the LSDA exchange-correlation functional, as opposed to more elaborate schemes such as the transverse spin-gradient scheme (*60*) not yet broadly available for such complex calculations, we always work with a locally collinear magnetic moment within each local frame-of-reference, in which we solve the single-site scattering problem for the effective potential around every atom. In particular, the spin magnetic moment given by the expectation value of the 4×4 $\beta\sigma_z$ Dirac matrix is free to adjust its magnitude to minimize the Kohn-Sham total energy, but not to vary the initially prescribed direction. These directions were chosen using semiclassical Heisenberg simulations as explained above in the section on Atomistic semiclassical Heisenberg model simulations.

When using this input for lower-level electronic structure calculations of total energy within the general scheme outlined above, results have been verified for a k-point convergence within the 3D/2D Brillouin zones respectively of the semi-infinite left and right regions, and of the interaction zone in the middle. The expansion in spherical harmonics has been evaluated up to $\Lambda_{max} = 3$, i.e., one level beyond the highest occupied d orbitals for Cu, Mn, and As elements in the atomic limit; and recovering comparable trends also when reaching larger angular momentum truncation up to $\Lambda_{max} = 5$ at a frozen potential approximation level. Basic tests of choosing a 40% larger interaction zone, up to 53.48 Å, have been used to verify adequate size for the SCF-DFT calculation.

Our results are summarized in Supplementary Fig. S14. For comparison, we performed analogous calculations for the antiferromagnetic CuMnAs and for ferromagnetic bcc Fe as a reference. For Fe, we obtain a result which is still consistent with the expectation from the semiclassical Heisenberg model: Since far below the micromagnetic domain wall width, the energy of the wall increases with decreasing wall width. For the last two points, the KKR-DFT energies are nearly identical. In contrast, the quantum mechanical KKR-DFT calculations in CuMnAs give a non-monotonous dependence of the energy on the domain wall width and a drop in the energy of the atomically sharp domain wall by one third of the highest energy corresponding to the second narrowest domain wall. This highlights the qualitative departure of the physics of narrow domain walls in CuMnAs antiferromagnet from the common understanding of magnetic textures based on the semiclassical spin models.

The comparison of panels S14B and 14C demonstrates, that the oscillatory dependence of the energy on the domain wall width in CuMnAs, and the significant energy drop for the atomically sharp domain wall, are not merely a consequence of the antiparallel moments in CuMnAs,

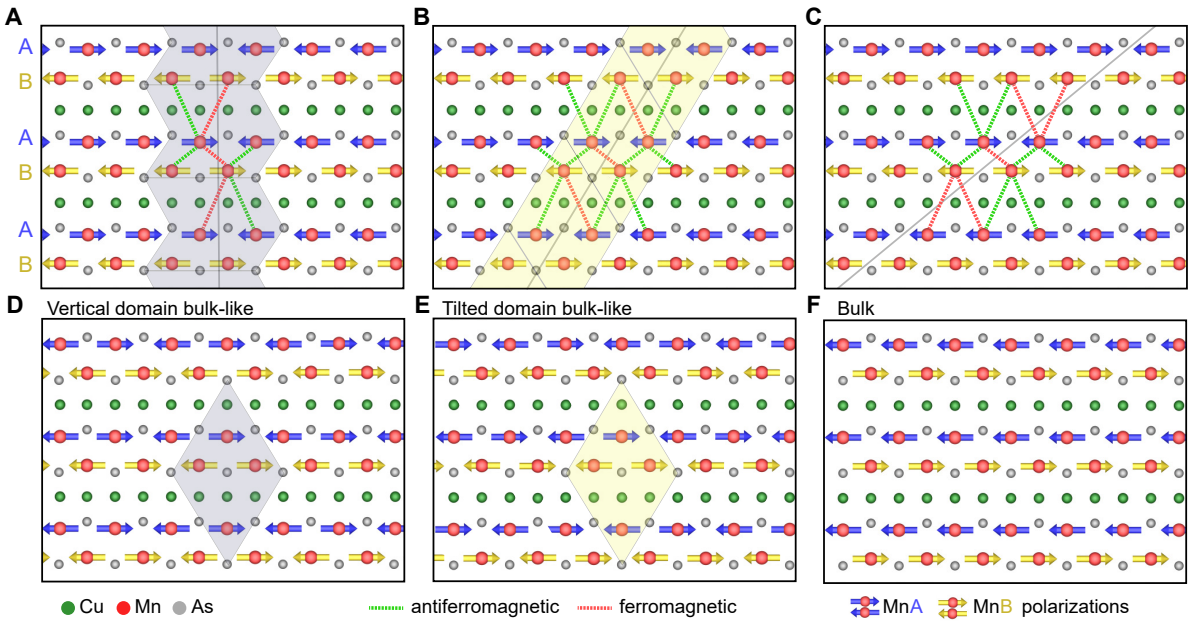

Figure S 15: DFT calculations of energies corresponding to different domain wall angles (**A,B,C**) Schematics of the vertical and tilted domain walls. Frustrated (ferromagnetic) bonds across the domain wall are highlighted by red dotted lines while unfrustrated (antiferromagnetic) bonds adjacent to the domain wall are highlighted by green dotted lines. The region of the domain wall in (A) and (B) is highlighted in grey and yellow, respectively. (**D,E**) Hypothetical bulk structures with spin configurations, as highlighted by the rhombus containing only near-neighbors, corresponding to domain walls in (A,B), respectively. The hypothetical bulk structures are constructed by periodically repeating the highlighted domain wall regions in (A,B). (**F**) Ground state spin configuration of bulk antiferromagnetic CuMnAs.

as opposed to the parallel moments in Fe. The antiparallel moment configuration enters both the ab initio DFT calculations, as well as the atomistic Heisenberg-model simulations in CuMnAs, shown in Supplementary Fig. S14B. In the latter case, however, the width dependence of the domain wall energy is monotonic. Therefore, the non-monotonic dependence results from a complex interplay of the antiparallel moments and the details of the electronic degrees of freedom, which the approximate atomistic Heisenberg-model simulations fail to describe properly, even on a qualitative level.

The above computational KKR-DFT method is applicable to a vertical [001]-orientation of the domain wall. To estimate the relative energy differences between vertical and tilted atomically sharp domain walls we first examine the number of (ferromagnetic) bonds across the domain wall aligned against the corresponding (antiferromagetic) bulk exchange field. These frustrated bonds are highlighted by red dotted lines in the schematic plots in Supplementary Fig. S15. In the vertical domain wall and the domain wall at an angle observed in experiment,

shown in Supplementary Figs. S15A,B, the number of frustrated bonds is the same, while the number increases for larger domain wall angles, as illustrated in Supplementary Fig. S15C. This makes domain walls with larger tilts starting from the one in Supplementary Fig. S15C unfavorable. To estimate the relative difference in energy between the domain walls in Supplementary Figs. S15A,B, we notice the different alignments of spins within the near-neighbor rectangle which determines the magnetic configuration of the bulk. These are shown in Supplementary Figs. S15D,E in which we constructed hypothetical bulk states with the spin configurations corresponding to domain walls in Supplementary Figs. S15A,B. The hypothetical bulk structures in Supplementary Figs. S15D,E are constructed by periodically repeating the highlighted domain wall regions in Supplementary Figs. S15A,B. We then performed DFT total energy calculations for these bulk states and obtained that the one corresponding to the tilted domain wall in Supplementary Fig. S15B, i.e. to the angle observed in experiment, has an energy which is about 20% lower than the bulk state with the spin configuration corresponding to the vertical domain wall in Supplementary Fig. S15A. These estimates of the domain wall energies indicate that the most stable domain wall angle is the one depicted in Supplementary Fig. S15B, consistent with experiment.

9 Potential pinning mechanisms of the atomically sharp domain walls in CuMnAs

9.1 Domain wall in the unperturbed crystal neighboring the anti-phase boundary domain wall

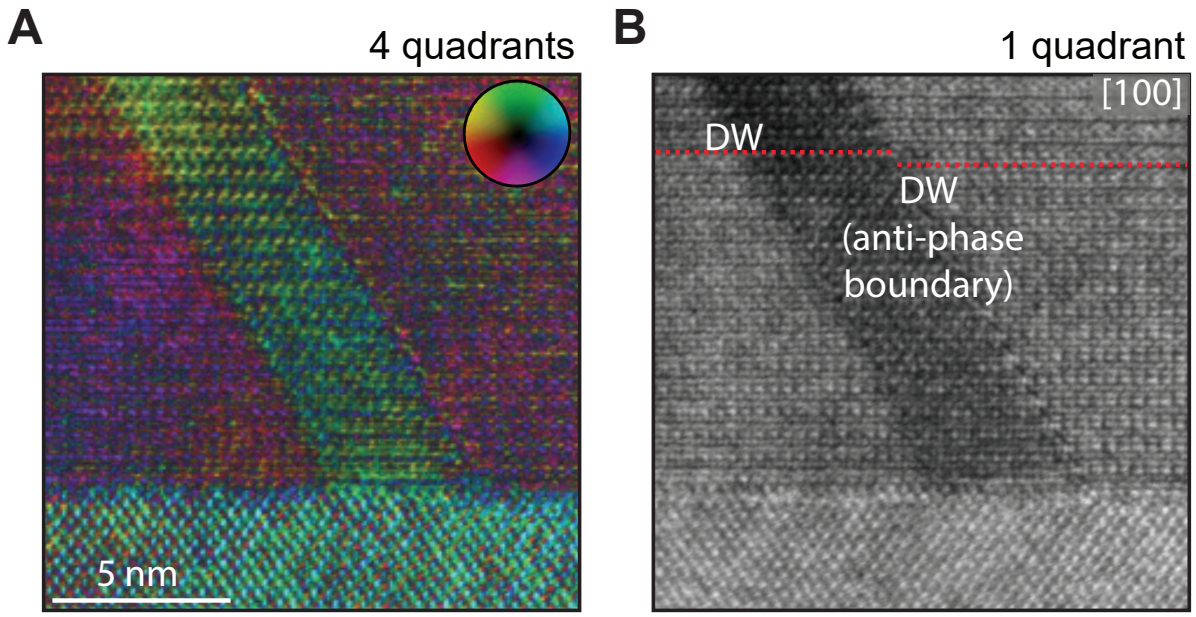

Figure S 16: Domain wall in the unperturbed crystal neighboring the anti-phase boundary domain wall. (**A**) DPC-STEM image acquired by a 4-quadrant detector in CuMnAs/GaP. (**B**) Same as (A) for the signal from one quadrant of the detector. The information from one quadrant makes it easier to follow the atomic lines, revealing that the right domain wall is at an anti-phase boundary while the left wall is in a part of the CuMnAs epilayer with no detectable crystal defect.

9.2 Scanning X-ray diffraction measurements of anti-phase boundary defects

Scanning X-ray diffraction measurements were performed at Nanomax beamline at MaxIV Laboratory in Lund Sweden. A 10 keV X-ray beam was focused to a full width at half maximum of 100 nm and used to study the local variations of diffraction features of our CuMnAs thin film. For this purpose the diffraction signal around the 003 Bragg reflection of CuMnAs was collected. An example of a three-dimensional diffraction signal of the 003 Bragg peak is shown in Supplementary Fig S17. Here, we observe streaks along directions perpendicular to the 011

planes, which reflect the presence of the anti-phase boundary defects. In the experiments the detector can be set to be sensitive to only selected features which then can be mapped out in real space by scanning the sample through the focused X-ray beam. Real-space maps of the sample produced only from the intensity of the observed streaks, i.e. signals reflecting the presence of anti-phase boundary defects, produce highly homogeneous images with no variations over the scanned areas. This indicates that anti-phase boundary defects have an average distance smaller than the X-ray beam, and cannot be resolved in the scanning diffraction map. We therefore conclude that such defects appear more frequently than approximately every 100 nm, which is also in line with the density observed in STEM measurements.

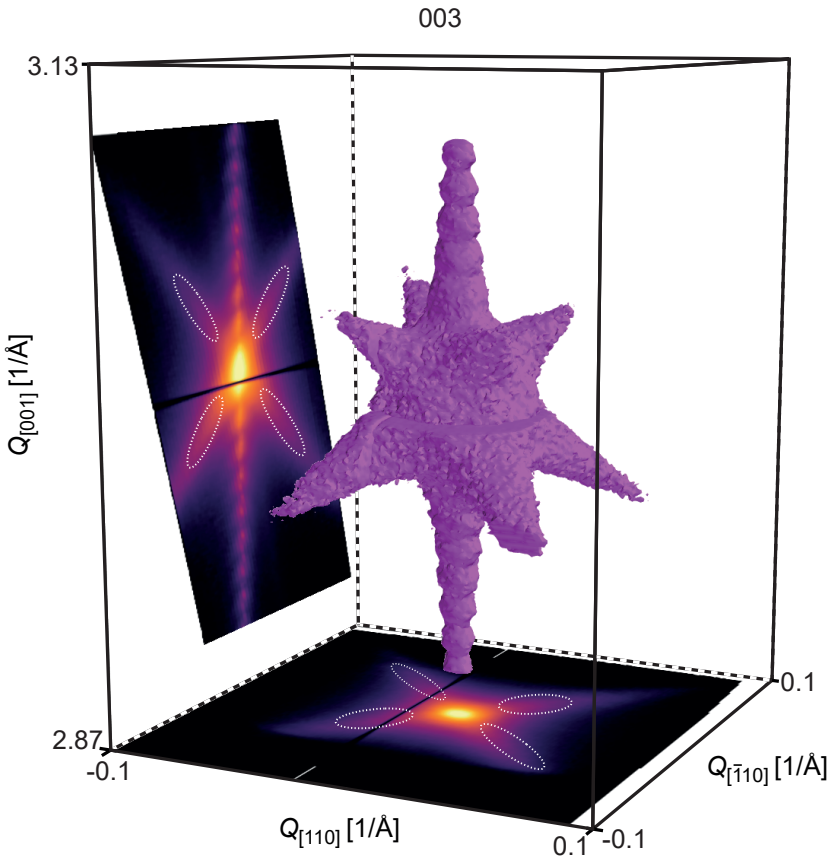

Figure S 17: XRD analysis of anti-phase boundary defects. Three-dimensional X-ray diffraction reciprocal space map of the 003 CuMnAs Bragg peak together with its projection onto the [110]/[1$\bar{1}$0] and [110]/[001] planes. Streaks related to the anti-phase boundary defects are highlighted by dotted white lines. The intensity variation along the [001] direction are Laue oscillations from the film thickness.

REFERENCES AND NOTES

1. F. Hellman, A. Hoffmann, Y. Tserkovnyak, G. S. D. Beach, E. E. Fullerton, C. Leighton, A. H. Mac Donald, D. C. Ralph, D. A. Arena, H. A. Dürr, P. Fischer, J. Grollier, J. P. Heremans, T. Jungwirth, A. V. Kimel, B. Koopmans, I. N. Krivorotov, S. J. May, A. K. Petford-Long, J. M. Rondinelli, N. Samarth, I. K. Schuller, A. N. Slavin, M. D. Stiles, O. Tchernyshyov, A. Thiaville, B. L. Zink, Interface-induced phenomena in magnetism. *Rev. Mod. Phys.* **89**, 025006 (2017).

2. S. Parkin, S.-H. Yang, Memory on the racetrack. *Nat. Nanotechnol.* **10**, 195–198 (2015).

3. S. J. Lloyd, J. C. Loudon, P. A. Midgley, Measurement of magnetic domain wall width using energy-filtered Fresnel images. *J. Microsc.* **207**, 118–128 (2002).

4. M. Bode, E. Y. Vedmedenko, K. von Bergmann, A. Kubetzka, P. Ferriani, S. Heinze, R. Wiesendanger, Atomic spin structure of antiferromagnetic domain walls. *Nat. Mater.* **5**, 477–481 (2006).

5. M. Enayat, Z. Sun, U. R. Singh, R. Aluru, S. Schmaus, A. Yaresko, Y. Liu, C. Lin, V. Tsurkan, A. Loidl, J. Deisenhofer, P. Wahl, Real-space imaging of the atomic-scale magnetic structure of Fe1+yTe. *Science* **345**, 653–656 (2014).

6. H. Zhao, S. Manna, Z. Porter, X. Chen, A. Uzdejczyk, J. Moodera, Z. Wang, S. D. Wilson, I. Zeljkovic, Atomic-scale fragmentation and collapse of antiferromagnetic order in a doped Mott insulator. *Nat. Phys.* **15**, 1267–1272 (2019).

7. P. Wadley, B. Howells, J. Železný, C. Andrews, V. Hills, R.P. Campion, V. Novák, K. Olejník, F. Maccherozzi, S.S. Dhesi, S.Y. Martin, T. Wagner, J. Wunderlich, F. Freimuth, Y. Mokrousov, J. Kuneš, J.S. Chauhan, M.J. Grzybowski, A.W. Rushforth, K.W. Edmonds, B.L. Gallagher, T. Jungwirth, Electrical switching of an antiferromagnet. *Science* **351**, 587–590 (2016).

8. M. Wang, C. Andrews, S. Reimers, O. J. Amin, P. Wadley, R. P. Campion, S. F. Poole, J. Felton, K. W. Edmonds, B. L. Gallagher, A. W. Rushforth, O. Makarovsky, K. Gas, M. Sawicki, D. Kriegner, J. Zubáč, K. Olejník, V. Novák, T. Jungwirth, M. Shahrokhvand, U. Zeitler, S. S. Dhesi, F.

Maccherozzi, Spin flop and crystalline anisotropic magnetoresistance in CuMnAs. *Phys. Rev. B* **101**, 094429 (2020).

9. N. H. Dekkers, H. de Lang, Differential phase contrast in a STEM. *Optik (Jena)* **41**, 452–456 (1974).

10. J. Chapman, P. Batson, E. Waddell, R. Ferrier, The direct determination of magnetic domain wall profiles by differential phase contrast electron microscopy. *Ultramicroscopy* **3**, 203–214 (1978).

11. K. Müller, F.F. Krause, A. Béché, M. Schowalter, V. Galioit, S. Löffler, J. Verbeeck, J. Zweck, P. Schattschneider, A. Rosenauer, Atomic electric fields revealed by a quantum mechanical approach to electron picodiffraction. *Nat. Commun.* **5**, 5653 (2014).

12. K. Shibata, J. Iwasaki, N. Kanazawa, S. Aizawa, T. Tanigaki, M. Shirai, T. Nakajima, M. Kubota, M. Kawasaki, H. S. Park, D. Shindo, N. Nagaosa, Y. Tokura, Large anisotropic deformation of skyrmions in strained crystal. *Nat. Nanotechnol.* **10**, 589–592 (2015).

13. M. Lohr, R. Schregle, M. Jetter, C. Wächter, K. Müller-Caspary, T. Mehrtens, A. Rosenauer, I. Pietzonka, M. Strassburg, J. Zweck, Quantitative measurements of internal electric fields with differential phase contrast microscopy on InGaN/GaN quantum well structures. *Phys. Status Solidi B* **253**, 140 (2016).

14. I. Lazić, E. G. Bosch, S. Lazar, Phase contrast STEM for thin samples: Integrated differential phase contrast. *Ultramicroscopy* **160**, 265–280 (2016).

15. T. Matsumoto, Y.G. So, Y. Kohno, H. Sawada, Y. Ikuhara, N. Shibata, Direct observation of Σ7 domain boundary core structure in magnetic skyrmion lattice. *Sci. Adv.* **2**, e1501280 (2016).

16. E. Yücelen, I. Lazić, E. G. T. Bosch, Phase contrast scanning transmission electron microscopy imaging of light and heavy atoms at the limit of contrast and resolution. *Sci. Rep.* **8**, 2676 (2018).

17. C. Chen, H. Li, T. Seki, D. Yin, G. Sanchez-Santolino, K. Inoue, N. Shibata, Y. Ikuhara, Direct determination of atomic structure and magnetic coupling of magnetite twin boundaries. *ACS Nano* **12**, 2662–2668 (2018).

18. J. A. Hachtel, J. C. Idrobo, M. Chi, Sub-angstrom electric field measurements on a universal detector in a scanning transmission electron microscope. *Adv. Struct. Chem. Imaging* **4**, 10 (2018).

19. A. Edström, A. Lubk, J. Rusz, Quantum mechanical treatment of atomic-resolution differential phase contrast imaging of magnetic materials. *Phys. Rev. B* **99**, 174428 (2019).

20. P. Wadley, S. Reimers, M. J. Grzybowski, C. Andrews, M. Wang, J. S. Chauhan, B. L. Gallagher, R. P. Campion, K. W. Edmonds, S. S. Dhesi, F. Maccherozzi, V. Novak, J. Wunderlich, T. Jungwirth, Current polarity-dependent manipulation of antiferromagnetic domains. *Nat. Nanotechnol.* **13**, 362–365 (2018).

21. J. Železný, H. Gao, K. Výborný, J. Zemen, J. Mašek, A. Manchon, J. Wunderlich, J. Sinova, T. Jungwirth, Relativistic néel-order fields induced by electrical current in antiferromagnets. *Phys. Rev. Lett.* **113**, 157201 (2014).

22. Z. Kašpar, M. Surýnek, J. Zubáč, F. Krizek, V. Novák, R. P. Campion, M. S. Wörnle, P. Gambardella, X. Marti, P. Němec, K. W. Edmonds, S. Reimers, O. J. Amin, F. Maccherozzi, S. S. Dhesi, P. Wadley, J. Wunderlich, K. Olejník, T. Jungwirth, Quenching of an antiferromagnet into high resistivity states using electrical or ultrashort optical pulses. *Nat. Electron.* **4**, 30–37 (2021).

23. T. Janda, J. Godinho, T. Ostatnicky, E. Pfitzner, G. Ulrich, A. Hoehl, S. Reimers, Z. Soban, T. Metzger, H. Reichlova, V. Novák, R. Campion, J. Heberle, P. Wadley, K. Edmonds, O. Amin, J. Chauhan, S. Dhesi, F. Maccherozzi, R. Otxoa, P. Roy, K. Olejnik, P. Němec, T. Jungwirth, B. Kaestner, J. Wunderlich, Magneto-Seebeck microscopy of domain switching in collinear antiferromagnet CuMnAs. *Phys. Rev. Mat.* **4**, 094413 (2020).

24. K. Müller-Caspary, F. F. Krause, T. Grieb, S. Löffler, M. Schowalter, A. Béché, V. Galioit, D. Marquardt, J. Zweck, P. Schattschneider, J. Verbeeck, A. Rosenauer, Measurement of atomic electric fields and charge densities from average momentum transfers using scanning transmission electron microscopy. *Ultramicroscopy* **178**, 62–80 (2017).

25. J. Barthel, Dr. Probe: A software for high-resolution STEM image simulation. *Ultramicroscopy* **193**, 1–11 (2018).

26. F. Krizek, Z. Kašpar, A. Vetushka, D. Kriegner, E.M. Fiordaliso, J. Michalicka, O. Man, J. Zubáč, M. Brajer, V.A. Hills, K.W. Edmonds, P. Wadley, R.P. Campion, K. Olejník, T. Jungwirth, V. Novák, Molecular beam epitaxy of CuMnAs. *Phys. Rev. Mat.* **4**, 014409 (2020).

27. F. Máca, J. Kudrnovský, V. Drchal, K. Carva, P. Baláž, I. Turek, Physical properties of the tetragonal CuMnAs: A first-principles study. *Phys. Rev. B* **96**, 094406 (2017).

28. J. Železný, P. Wadley, K. Olejník, A. Hoffmann, H. Ohno, Spin transport and spin torque in antiferromagnetic devices. *Nat. Phys.* **14**, 220–228 (2018).

29. P. Němec, M. Fiebig, T. Kampfrath, A. V. Kimel, Antiferromagnetic opto-spintronics. *Nat. Phys.* **14**, 229–241 (2018).

30. O. Gomonay, V. Baltz, A. Brataas, Y. Tserkovnyak, Antiferromagnetic spin textures and dynamics. *Nat. Phys.* **14**, 213–216 (2018).

31. L. Šmejkal, T. Jungwirth, in *Topology in Magnetism*, J. Zang, V. Cros, A. Hoffmann, Eds. (Springer International Publishing, 2018), pp. 267–298.

32. R. A. Duine, K.-J. Lee, S. S. P. Parkin, M. D. Stiles, Synthetic antiferromagnetic spintronics. *Nat. Phys.* **14**, 217–219 (2018).

33. V. Baltz, A. Manchon, M. Tsoi, T. Moriyama, T. Ono, Y. Tserkovnyak, Antiferromagnetic spintronics. *Rev. Mod. Phys.* **90**, 015005 (2018).

34. S. A. Siddiqui, J. Sklenar, K. Kang, M. J. Gilbert, A. Schleife, N. Mason, A. Hoffmann, Metallic antiferromagnets. *J. Appl. Phys.* **128**, 040904 (2020).

35. J. Zubáč, Z. Kašpar, F. Krizek, T. Förster, R. P. Campion, V. Novák, T. Jungwirth, K. Olejník, Hysteretic effects and magnetotransport of electrically switched CuMnAs. *Phys. Rev. B* **104**, 184424 (2021).

36. A. Kurenkov, S. Fukami, H. Ohno, Neuromorphic computing with antiferromagnetic spintronics. *J. Appl. Phys.* **128**, 010902 (2020).

37. A. V. Kimel, M. Li, Writing magnetic memory with ultrashort light pulses. *Nat. Rev. Mat.* **4**, 189–200 (2019).

38. O. Gomonay, T. Jungwirth, J. Sinova, High antiferromagnetic domain wall velocity induced by néel spin-orbit torques. *Phys. Rev. Lett.* **117**, 017202 (2016).

39. P. Wadley, K. W. Edmonds, M. R. Shahedkhah, R. P. Campion, B. L. Gallagher, J. Železný, J. Kuneš, V. Novák, T. Jungwirth, V. Saidl, P. Němec, F. Maccherozzi, S. S. Dhesi, Control of antiferromagnetic spin axis orientation in bilayer Fe/CuMnAs films. *Sci. Rep.* **7**, 11147 (2017).

40. C. Meyer (2019), Nion Swift (version 0.14.08), https://github.com/nion-software/nionswift.

41. M. J. Grzybowski, P. Wadley, K. W. Edmonds, R. Beardsley, V. Hills, R. P. Campion, B. L. Gallagher, J. S. Chauhan, V. Novak, T. Jungwirth, F. Maccherozzi, S. S. Dhesi, Imaging current-induced switching of antiferromagnetic domains in CuMnAs. *Phys. Rev. Lett.* **118**, 057701 (2017).

42. J. Bürger, T. Riedl, J. K. Lindner, Influence of lens aberrations, specimen thickness and tilt on differential phase contrast STEM images. *Ultramicroscopy* **219**, 113118 (2020).

43. P. Blaha, K. Schwarz, G. K. H. Medsen, D. Kvasnicka, J. Luitz, *WEIN2K, An Augmented Plane Wave + Local Orbitals Program for Calculating Crystal Properties* (Vienna University of Technology, 2001).

44. A. Edström, A. Lubk, J. Rusz, Magnetic effects in the paraxial regime of elastic electron scattering. *Phys. Rev. B* **94**, 174414 (2016).

45. A. Edström, A. Lubk, J. Rusz, Elastic scattering of electron vortex beams in magnetic matter. *Phys. Rev. Lett.* **116**, 127203 (2016).

46. T. Malis, S. Cheng, R. Egerton, EELS log-ratio technique for specimen-thickness measurement in the TEM.*J. Electron Microsc. Tech.* **8**, 193–200 (1988).

47. G. P. Müller, M. Hoffmann, C. Dißelkamp, D. Schürhoff, S. Mavros, M. Sallermann, N. S. Kiselev, H. Jónsson, S. Blügel, Spirit: Multifunctional framework for atomistic spin simulations. *Phys. Rev. B* **99**, 224414 (2019).

48. A. Liechtenstein, M. Katsnelson, V. Antropov, V. Gubanov, Local spin density functional approach to the theory of exchange interactions in ferromagnetic metals and alloys. *J. Mag. Magnetic Mat.* **67**, 65–74 (1987).

49. H. Ebert, S. Mankovsky, D. Ködderitzsch, P. J. Kelly, Ab initio calculation of the gilbert damping parameter via the linear response formalism. *Phys. Rev. Lett.* **107**, 066603 (2011).

50. P. Strange, *Relativistic Quantum Mechanics* (Cambridge University Press, 2010).

51. H. Eschrig, M. Richter, I. Opahle, in *Relativistic Electronic Structure Theory*, P. Schwerdtfeger, Ed. (Elsevier, 2004), chap. 12, pp. 723–776.

52. S. H. Vosko, L. Wilk, M. Nusair, Accurate spin-dependent electron liquid correlation energies for local spin density calculations: A critical analysis. *Can. J. Phys.* **58**, 1200–1211 (1980).

53. D. Wagenknecht, K. Výborný, K. Carva, I. Turek, Antiferromagnetic CuMnAs: Ab initio description of finite temperature magnetism and resistivity. *J. Mag. Magnetic Mat.* **513**, 167078 (2020).

54. P. W. Ilja Turek, V. Drchal, J. Kudrnovský, M. Sob, *Electronic Structure of Disordered Alloys, Surfaces and Interfaces* (Springer, 1997).

55. G. Kresse, J. Furthmüller, Efficiency of ab-initio total energy calculations for metals and semiconductors using a plane-wave basis set. *Comput. Mater. Sci.* **6**, 15–50 (1996).

56. K. Koepernik, H. Eschrig, Full-potential nonorthogonal local-orbital minimum-basis band-structure scheme. *Phys. Rev. B* **59**, 1743 (1999).

57. P. Wadley, A. Crespi, J. Gázquez, M.A. Roldán, P. García, V. Novak, R. Campion, T. Jungwirth, C. Rinaldi, X. Martí, V. Holy, C. Frontera, J. Rius, Obtaining the structure factors for an epitaxial film using Cu x-ray radiation. *J. Appl. Cryst.* **46**, 1749–1754 (2013).

58. B. Ujfalussy, L. Szunyogh, P. Weinberger, J. Kollár, in *Metalllic Alloys: Experimental and Theoretical Prospectives*, J. Faulkner, R. Jordan, Eds. (NATO Advanced Study Institutes Series, 1994), p. 301.

59. K. Wildberger, R. Zeller, P. Dederichs, Screened KKR-Green's-function method for layered systems. *Phys. Rev. B* **55**, 10074 (1997).

60. F. G. Eich, E. K. Gross, Transverse spin-gradient functional for noncollinear spin-density-functional theory. *Phys. Rev. Lett.* **111**, 156401 (2013).